Charge–discharge behavior of Sn–Ni alloy film electrodes in an intermediate temperature ionic liquid for the electrolyte of a sodium secondary battery

Takayuki Yamamoto [a], Toshiyuki Nohira [b,*], Rika Hagiwara [a,*], Atsushi Fukunaga [c], Shoichiro Sakai [c], and Koji Nitta [c]

[a] Graduate School of Energy Science, Kyoto University, Yoshida-honmachi, Sakyo-ku, Kyoto, 606-8501, Japan

[b] Institute of Advanced Energy, Kyoto University, Gokasho, Uji, 611-0011, Japan

[c] Sumitomo Electric Industries Ltd., 1-1-3 Shimaya, Konohana-ku, Osaka, 554-0024, Japan

* Corresponding Authors:

E-mail: nohira.toshiyuki.8r@kyoto-u.ac.jp, hagiwara@energy.kyoto-u.jp,

Tel: +81-774-38-3500, Fax: +81-774-38-3499 (T. Nohira), Tel: +81-75-753-5822, Fax: +81-75-753-5906 (R. Hagiwara)

Abstract

Sn–Ni alloy films were prepared by annealing tin-coated nickel foils at 463 K for 0–25 h, and their charge–discharge characteristics as negative electrodes for sodium secondary batteries were studied in an intermediate temperature ionic liquid Na[FSA]–K[FSA] (FSA = bis(fluorosulfonyl)amide) at 363 K. As a result, a Sn–Ni film without annealing retained a reversible capacity of 343 mAh $(g\text{-}Sn)^{-1}$ after 100 charge–discharge cycles. In contrast, the annealed films had lower capacities and poorer cycleability. Possible mechanisms to understand the cycling performance were identified by X-ray diffraction and field-emission scanning electron microscopy studies.

Keywords: Sodium secondary battery; Ionic liquid; Sn–Ni alloy; Negative electrode; Cycleability

1. Introduction

Since the reduction of CO_2 emission is one of our unavoidable issues to prevent global warming, it is necessary to establish a new sustainable energy supply system that is free from fossil fuel resources. Renewable energy sources such as solar power and wind power are promising solutions to the aforementioned problem. However, because energy output from these sources fluctuates with weather, they must be combined with electrical energy storage (EES) devices to ensure stable power supply. In the last 20 years, lithium-ion batteries (LIBs) have been widely used in mobile phones and laptops because of their high energy densities. Furthermore, LIBs are expected to be increasingly used for electric vehicles (EV) and stationary energy storage devices in offices and homes. However, lithium resources are mostly limited to South America. Thus, there is a risk of supply instability that could lead to increasing prices. For these reasons, especially in the last decade, alternative batteries utilizing more abundant resources such as sodium have been investigated [1–4]. Moreover, it has similar chemistry as lithium and a relatively low standard redox potential (–2.71 V vs. SHE) as compared to lithium (–3.05 V vs. SHE). Consequently, sodium can be used to produce batteries of low cost and high energy density.

Recent studies on ambient temperature sodium secondary batteries have mainly

used sodium salts dissolved in either organic [5,6] or aqueous solutions [7] as electrolytes. However, safety issues arise from the use of organic solvents due to their high volatility and flammability. Furthermore, the use of aqueous solutions limits the energy density of the battery because of the narrow electrochemical window. Therefore, we have focused on using ionic liquids as electrolytes for sodium secondary batteries [8–20]. Ionic liquids possess high safety such as nonflammability and negligible volatility, and also have wide electrochemical windows. For example, Na[FSA]–K[FSA] ionic liquid (Na[FSA] : K[FSA] = 56:44 in molar ratio, m.p. = 334 K; FSA = bis(fluorosulfonyl)amide)) is a promising electrolyte for sodium secondary batteries [11,13], and several positive electrodes such as $NaCrO_2$ and $Na_2FeP_2O_7$ show good cycling performance in this ionic liquid at 353–363 K [13–15]. However, highly reactive sodium metal was used as a negative electrode, and the development of safer negative electrode materials with high energy densities was a remaining issue.

We chose tin as an alternative negative electrode material because of the safety and the high theoretical capacity (847 mAh $(g\text{-}Sn)^{-1}$ for the sodium-richest phase $Na_{15}Sn_4$ [16,17]). We have investigated the cycle performance and reaction mechanism of tin-based negative electrodes in Na[FSA]–K[FSA] ionic liquid at 363 K [18–20]. However, tin-coated aluminum foils with ca. 10 μm thickness of tin showed rapid

capacity fade within the first ten cycles (from 729 to 121 mAh $(g\text{-}Sn)^{-1}$) [18]. This capacity loss is due to the pulverization of the active materials, resulting from the large volume changes during cycling. Consequently, the active material particles lose electrical contact with both neighboring particles and the current collector. This pulverization represents the typical degradation behavior of alloy-based negative electrode materials for lithium-ion batteries [21]. Therefore, with an aim to improve cycleability, tin-coated copper foils with ca. 1 μm thickness of tin (hereinafter, labeled "Sn–Cu films") were prepared by electrodeposition, followed by annealing at 463 K to form an intermetallic buffer layer (Cu_6Sn_5 and Cu_3Sn) [20]. A Sn–Cu film annealed for 4 h had a stable reversible capacity of approximately 100 mAh $(g\text{-}Sn)^{-1}$ and high cycling stability for 1000 cycles. However, its reversible capacity was found to be lower than the theoretical capacity of tin.

In recent years, there have been increasing reports on tin-based negative electrodes for sodium batteries that use organic electrolytes and function at room temperature [22–38]. In addition to pure tin [22–25], several systems such as Sn–M (M = Sb, Cu, Co, Ge, Ni, and Se) [26–32], SnO_x [33,34], SnS_x [35,36], and Sn_4P_3 [37,38] have been investigated to improve cycle performance. For example, Ni_3Sn_2 nanoparticles deliver a stable capacity of 270 mAh g^{-1} at 1C rate after 300 cycles [31].

In lithium batteries, improved cycle performances of co-electrodeposited Sn–Ni alloy thin films have been reported [39,40]. Thus, it is well expected that Sn–Ni system also gives good charge–discharge characteristics for sodium secondary batteries. We especially focused on the electrodeposited tin film on nickel substrate because a coherent and strong interface between tin and nickel could be easily prepared and it would prevent the delamination of the active material layer from the substrate, leading to the high capacity and cycleability. Moreover, since this simple electrode structure does not require conductive agents or binders, a higher capacity is expected compared with the conventional mixed electrodes. By examining this material, as in the case of Sn–Cu alloy film, it is also expected to elucidate the role of the Sn–Ni alloy buffer [20,41,42].

In this study, we investigated the cycling performances of Sn–Ni alloy films, prepared by annealing tin-coated nickel foils as the negative electrode for sodium secondary batteries, using Na[FSA]–K[FSA] ionic liquid electrolyte at 363 K. Sn–Ni films were prepared with different annealing times (from 0 to 25 h) to evaluate the effect of the alloying degree on the charge–discharge performance. The electrodes were analyzed by X-ray diffraction (XRD) and field-emission scanning electron microscopy (FE-SEM) both before and after the charge–discharge tests. Furthermore, the cycling

mechanism was discussed.

2. Experimental

2.1 Reagents and their handling

Na[FSA] (99+%) and K[FSA] (99+%) were purchased from Mitsubishi Materials Electronic Chemicals Co., Ltd. The salts were dried under vacuum at 353 K for 48 h before use. The Na[FSA]–K[FSA] eutectic salt (x(Na[FSA]) = 0.56 [11]) was prepared by grinding the two salts in a mortar.

Tin-coated nickel foils were prepared by electrodeposition of tin onto nickel foils. The loading mass of tin was determined via inductively coupled plasma-atomic emission spectroscopy (ICP-AES). Before electrochemical measurements, the Sn–Ni films were dried under vacuum at 363 K for 48 h, and some of them were annealed at 463 K under vacuum. Rotary vane pumps were used for both drying and annealing processes, and the achieved vacuum levels were approximately 1 Pa. Annealing times were set to 2, 10, or 25 h. After the annealing process, the Sn–Ni films were transferred to an argon-filled glovebox without air exposure.

2.2 Electrochemical measurements and analysis

Galvanostatic charge–discharge of the test cells was conducted under argon using electrochemical measurement apparatus (VSP, Bio-Logic Co., or 580-type battery cycler, Toyo Co.) in a two-electrode cell (Tomcell Japan Co., Ltd.). A two-ply glass-fiber filter paper (Whatman, GF/A, 260 μm), used as a separator, was vacuum-impregnated with the electrolyte prior to the test. Based on the ICP-AES results, Sn–Ni alloy films with tin loading masses between 0.67 and 0.85 mg cm^{-2} (corresponding to tin thicknesses of 0.92 to 1.16 μm) were selected and used as the working electrodes. The counter electrode was composed of Na metal (99.85%, Sigma Aldrich Inc.). The charge–discharge rate was set to 84.7 mA $(g\text{-}Sn)^{-1}$, corresponding to a rate of C/10. Cut-off voltages were 0.005 and 1.200 V, and the operating temperature was 363 K for all the tests. The two-electrode cell was heated using a mantle heater, and the temperature of the cell was monitored using a thermocouple and maintained at 363 K.

To characterize the Sn–Ni alloy films before and after charge–discharge tests, X-ray diffraction (XRD) analysis was applied to identify the phases in the films, using an X-ray diffractometer (SmartLab, Rigaku Co.; Cu-Kα radiation (λ = 0.15418 nm)) equipped with a 1D high-speed detector (D/teX Ultra, Rigaku Co.) with a nickel filter. The elemental compositions and chemical states of Sn–Ni alloy films were investigated by X-ray photoelectron spectroscopy (XPS; JPS-9010, JEOL) combined with argon-ion

etching. The surfaces and cross-sections of the films were observed by a field-emission scanning electron microscope (FE-SEM; SU-8020, Hitachi or JSM-7600F, JEOL). Before the cross-sectional SEM observation, a cross-section polisher (CP; IB090-20, JEOL) was used to cut the Sn–Ni alloy films. After the charge–discharge tests, all the cells were disassembled and the Na[FSA]–K[FSA] salts on the surfaces of Sn–Ni films were removed by soaking the samples in dehydrated and deoxidized tetrahydrofuran (water content < 10 ppm, oxygen content < 1 ppm; Wako Pure Chemical Industries, Ltd.). These manipulations were conducted in the argon-filled glovebox. Finally, the samples were transferred to the analysis or work chambers of XRD, CP and FE-SEM without air exposure by using transfer vessels.

3. Results and discussion

3.1 Characterization of Sn–Ni films before charge–discharge tests

3.1.1 XRD

Fig. 1 shows the XRD patterns of the Sn–Ni films before charge–discharge tests. A Sn–Ni film without annealing at 463 K (hereinafter, labeled “0h-annealed film”) is found to consist of four phases, *i.e.*, β-Sn, $NiSn_3$, Ni_3Sn_4, and the Ni current collector. $NiSn_3$ is a metastable intermetallic compound, and is obtained by electrodeposition of

tin on nickel [43] or by co-electrodeposition of tin and nickel [39,40]. Since the Ni_3Sn_4 phase peak intensity is weak, the Ni_3Sn_4 phase is a minor component. In the 2h-annealed film, the intensities of β-Sn peaks become weaker, and those of Ni_3Sn_4 peaks become stronger. Furthermore, the preferred orientation of the metastable $NiSn_3$ phase changes to (00*l*). In the 10h-annealed film, the metastable $NiSn_3$ phase disappears whereas the β-Sn and Ni_3Sn_4 phases remain. In the previous report [43], the disappearance of the metastable $NiSn_3$ phase was observed at temperatures higher than 433 K. Finally, after 25 h annealing, the β-Sn phase totally disappears and only Ni_3Sn_4 phase is observed except for Ni current collector.

3.1.2 XPS

Fig. 2 summarizes XPS depth profiles of the Sn–Ni films before charge–discharge tests. For all the films without etching, peaks from the Sn $3d_{5/2}$ are observed, indicating the oxidized state of tin (486.5 eV for Sn^{2+} or 486.9 eV for Sn^{4+}), and there is no clear difference in their intensities. Since no Ni $2p_{3/2}$ peaks are observed, the surfaces of Sn–Ni films are likely to be covered by a SnO_x layer. After 2 seconds etching, the Sn $3d_{5/2}$ peaks shift to the Sn^0 position, indicating the removal of the oxide layer. The 0h- and 2h-annealed films show stronger Sn $3d_{5/2}$ peaks than other films. A clear peak at

around 853 eV, ascribed to Ni $2p_{3/2}$, is observed for the 10h-annealed film, suggesting the presence of nickel near the surface. In contrast, there are no obvious peaks in the 0h- or 2h-annealed films. For the 25h-annealed film, a higher intensity Ni $2p_{3/2}$ peak is observed. In summary, stronger Ni $2p_{3/2}$ and weaker Sn $3d_{5/2}$ peaks are observed for Sn–Ni films with increasing annealing time. Moreover, with further etching (10–120 seconds), the Ni $2p_{3/2}$ peak intensities of all the films become stronger, and their Sn $3d_{5/2}$ peak intensities become weaker. Therefore, the formation of Ni–Sn alloy proceeds from the Sn/Ni interface towards the top surface of the β-Sn layer.

3.1.3 Cross-sectional FE-SEM

To investigate the morphologies of the Sn–Ni alloy phases, cross-sectional SEM observation was conducted. As shown in Fig. 3a, in the 0h-annealed film, an electrodeposited β-Sn phase (white region) can be seen on the nickel film (black region). However, on examination of the enlarged view of the β-Sn layer (Fig. 3b), a non-uniform morphology is observed. According to the previous report on the growth of Ni–Sn alloys [43], a laminar Ni_3Sn_4 layer was observed on the nickel substrate and needle-like $NiSn_3$ pillars coexisted in the β-Sn layer. Considering the fact that Ni_3Sn_4 and $NiSn_3$ phases were detected by XRD, it is reasonable to conclude that the thin layer

(ca. 100 nm thickness) adjacent to nickel substrate and the needle-like structures penetrating the β-Sn layer correspond to the Ni_3Sn_4 and metastable $NiSn_3$ phases, respectively. In the 2h-annealed film (Fig. 3c), the area of the Ni–Sn alloy layer clearly increases, and the needle-like morphology disappears, consistent with the XRD results (see Fig. 1).]In the 10h-annealed film, most of the β-Sn region has transformed into the Ni_3Sn_4 phase (Fig. 3d), and has disappeared in the 25h-annealed film (Fig. 3e).

3.2 Charge–discharge behavior of Sn–Ni films

Fig. 4a shows the initial charge–discharge curves of Sn–Ni films. For all films except the 25h-annealed film, several plateaus are observed for both charge and discharge processes below 0.6 V. According to our previous studies [18–20], these plateaus are assigned to the sodiation/desodiation behavior of β-Sn. Initial discharge (desodiation) capacities are 605, 305, 121, and 2 mAh $(g\text{-}Sn)^{-1}$ for the 0h-, 2h-, 10h-, and 25h-annealed films, respectively, *i.e.*, lower initial capacities are obtained for Sn–Ni films with longer annealing times. Combined with the XRD results (Fig. 1), these results suggest that the Ni_3Sn_4 phase formed by annealing has an extremely low activity with sodium. In contrast, in lithium-ion batteries [39,40], Ni_3Sn_4 is reported to exhibit high initial capacities (500–600 mAh g^{-1}).

The cycling performances of the Sn–Ni films are summarized in Fig. 4b. Although the discharge capacity of the 0h-annealed film decreases from 605 to 226 mAh $(g\text{-}Sn)^{-1}$ in the first ten cycles, it gradually increases again to 343 mAh $(g\text{-}Sn)^{-1}$ after 100 cycles. A similar phenomenon has been observed previously for tin-based negative electrodes in both lithium [39,44] and sodium [20] secondary batteries. The capacity fade in early cycles is explained by the pulverization of the active material, in the same manner as our previous reports [18,20]. Concerning capacity recovery, the mechanism is discussed later in detail based on the results of XRD and SEM analyses carried out after charge–discharge tests.

In contrast to the 0h-annealed film, the capacities of the 2h- and 10h-annealed films rapidly decrease to 36 and 24 mAh $(g\text{-}Sn)^{-1}$, respectively, within the first ten cycles. In the case of Sn–Cu films [20], the behavior is different; that is, the 4h-annealed film exhibited the most stable and reversible capacity of ca. 100–120 mAh $(g\text{-}Sn)^{-1}$. These results indicate that Ni_3Sn_4 layers in the 2h- and 10h-annealed films do not buffer the strain generated by the large volume changes of Na–Sn alloys during alloying and dealloying. For the 25h-annealed film, very small capacities lower than 5 mAh $(g\text{-}Sn)^{-1}$ are observed for 100 cycles, indicating that the Ni_3Sn_4 phase is inactive towards sodium, as mentioned above.

3.3 Characterization of Sn–Ni films after charge–discharge test

3.3.1 XRD

Fig. 5 compares the XRD patterns of the Sn–Ni films before and after charge–discharge tests. For the 0h-annealed film (Figs. 5a and 5b), the diffraction peak of β-Sn (211, 45.0°) is strong before charge–discharge test, indicative of its preferred orientation. After the test, the diffraction pattern changes to that of the reported powder pattern. Moreover, after the test, reflections due to the $NiSn_3$ phase disappear, and those due to the Ni_3Sn_4 phase become more intense. Here, it is likely that the metastable $NiSn_3$ phase reacts with sodium, transforming into Ni_3Sn_4 and Na–Sn alloy phases according to the following equation:

$$3\ NiSn_3 + x\ Na^+ + x\ e^- \rightarrow Ni_3Sn_4 + Na_xSn_5 \qquad (1)$$

For the 2h-annealed film (Figs. 5c and 5d), the preferred orientation of β-Sn phase disappears, and diffraction peaks of $NiSn_3$ phase vanish as in the case of the 0h-annealed film. The Ni_3Sn_4 phase peak intensities are almost unchanged, indicating that Ni_3Sn_4 phase is inactive to sodium. For the 10h-annealed film (Figs. 5e and 5f), similar changes to those of the 2h-annealed film is observed after the test. For the 25h-annealed film (Figs. 5g and 5h), which is entirely constituted of the inactive Ni_3Sn_4

phase, no changes are observed after the test.

3.3.2 Surface FE-SEM

Fig. 6 summarizes the selected surface FE-SEM images of Sn–Ni films before and after charge–discharge tests. As shown in Figs. 6a, 6c, 6e, and 6g, all films are smooth and flat before the charge–discharge tests. For the 0h-annealed film, the surface becomes rough after 100 cycles of charge–discharge (Fig. 6b). The surfaces of the 2h- and 10h-annealed films were much rougher (Figs. 6d and 6f), suggesting that the active materials pulverize and become electrically isolated. No noticeable change is observed on the surface of the 25h-annealed film (Fig. 6h), corresponding with its extremely low reversible capacity. These results are consistent with the cycleability of the Sn–Ni films.

3.3.3 Cross-sectional FE-SEM

To further investigate the morphologies of Sn–Ni alloys, cross-sectional SEM observation was conducted, as shown in Fig. 7. Figs. 7a and 7b show the cross-sectional SEM images of the 0h-annealed film after the charge–discharge test. Compared to the morphology before the test (see Figs. 3a and 3b), the thin Ni_3Sn_4 layer (white) adjacent to the nickel substrate retains its morphology and remains almost unreacted after the test.

As mentioned in the introduction, the formation of such coherent interface is important for tin film electrodes to prevent the delamination of the active material layer from the substrate. Moreover, the needle-like morphology of $NiSn_3$ phase disappears, and small white particles (ca. 100 nm in diameter) are uniformly dispersed over the Ni_3Sn_4 layer. In contrast, as shown in Figs. 7c and 7d, a roughened surface and large pores are observed in the 2h-annealed film, corresponding to the surface SEM observations (see also Fig. 6). Furthermore, many cracks are observed in the thicker Ni_3Sn_4 layer (ca. 500 nm in thickness). Ni_3Sn_4 is less flexible and has a lower fracture toughness than Cu–Sn alloys (Cu_6Sn_5 and Cu_3Sn), and even thin films of 0.7 μm thickness easily collapses [45,46]. For the 10h-annealed film (Fig. 7e), similar fracture of the Ni_3Sn_4 region is observed, corresponding to its low reversible capacity. Incidenally, in the cases of lithium batteries [39,40], the Ni_3Sn_4 films were reported to react with lithium and show good capacity retention. In these cases, the Ni_3Sn_4 films were prepared by the co-electrodeposition of nickel and tin, and no annealing treatment was conducted. Thus, the particles size of Ni_3Sn_4 was as small as approximately 100 nm [39], which would have prevented the collapse of the electrode. As shown in Fig. 7f, in the 25h-annealed film, any remarkable changes such as the collapse of the Ni_3Sn_4 layer are not observed, indicating the electrical isolation of Ni_3Sn_4 layer does not occur. Therefore, it naturally

leads to the conclusion that Ni_3Sn_4 has little activity for sodium, consistent with the results of charge–discharge tests (see also Fig. 4).

3.4 Mechanism of cycle characteristics for Sn–Ni films

3.4.1 0h-annealed film

As described in Section 3.2, the capacity declines in the 0h-annealed film within the first ten cycles of charge–discharge. After that, the capacity has gradually recovered. Concerning the capacity recovery after ten cycles, three effects are likely to be involved.

Firstly, the Ni_3Sn_4 thin layer retains its morphology and, therefore, electrical contact between the active material layer and the Ni current collector, even after 100 cycles. Generally, it is important for tin film electrode to maintain a coherent interface between the active and inactive regions because the degradation of the electrode usually occurs due to the delamination of the former from the latter [20,41,42].

The second effect is the increase in effective surface area of the active material. As shown in Fig. 3b, the average thicknesses of the inactive Ni_3Sn_4 and active β-Sn layers (containing needle-like $NiSn_3$) of the 0h-annealed film are approximately 100 nm and 1 μm, respectively. The $NiSn_3$ phase in the β-Sn layer is electrochemically active toward sodium, as mentioned in Subsection 3.3.1. Therefore, more than 90% of the tin in this

film reacts with sodium. However, the observed initial discharge capacity of 605 mAh $(g\text{-}Sn)^{-1}$ is as low as 71% of the theoretical capacity for β-Sn (847 mAh $(g\text{-}Sn)^{-1}$). Thus, at this point, it is reasonable to consider that some of β-Sn regions such as the inner part of β-Sn grains and/or particles remain unreacted. After several cycles, the particle sizes decrease and microcracks form in the Sn–Ni film. Then, the effective surface area increases and sodium ions in the electrolyte can infiltrate the remaining unreacted β-Sn. In this way, these regions contribute to the observed capacities after the first ten cycles of charge–discharge.

The third effect is the recovery of electrical contact of electrically isolated β-Sn particles formed during the initial cycles. As shown in Fig. 7b, small particles are homogeneously distributed on the Ni_3Sn_4 layer of the 0h-annealed film. It is reasonable to assume that some of these particles are Ni_3Sn_4, formed by electrochemical reaction of the needle-like $NiSn_3$ phase (see also Subsection 3.3.1). Owing to these dispersed Ni_3Sn_4 particles, a part of β-Sn region maintains electrical contact with the Ni current collector, preventing fatal degradation of the Sn–Ni film electrode. Furthermore, since the annealing temperature (463 K) and melting point of tin (505 K) are close to the operation temperature (363 K), the diffusion of tin is fast enough for isolated β-Sn particles to be electrically reconnected to the other β-Sn particles and/or Ni_3Sn_4 particles

even at 363 K. Thus, those electrically reconnected tin particles gradually contribute to the capacity after the first ten cycles of charge–discharge.

3.4.2 2h-, 10h-, 25h-annealed films

For the 2h-annealed film, the discharge capacity has drastically decreased during the first ten cycles of charge–discharge. After that, in contrast to the 0h-annealed film, the capacity recovery is not observed. This poor cycleability is explained as follows. Firstly, significant pulverization of β-Sn occurs because there are few dispersed small Ni_3Sn_4 particles in the β-Sn layer. Secondly, as shown in Fig. 7d, the collapsed Ni_3Sn_4 layer loses electrical contact, leading to electrical isolation of the active material above this layer. A similar mechanism is applicable to the 10h-annealed film. For the 25h-annelaed film, as discussed above, very low capacities are observed during 100 cycles of charge–discharge because the major phase, Ni_3Sn_4, is inactive with sodium.

4. Conclusions

In this study, with the aim of developing a new negative electrode that has high capacity and good cycleability, Sn–Ni alloy thin films were prepared by annealing tin-coated nickel foils at 463 K for 0–25 h, and their charge–discharge behaviors were

investigated in an intermediate temperature ionic liquid, Na[FSA]–K[FSA], at 363 K.

The 0h-annealed film was initially composed of β-Sn, needle-like $NiSn_3$, and laminar Ni_3Sn_4 phases, and showed the best cycleability and retained its reversible capacity of 343 mAh $(g\text{-}Sn)^{-1}$ even after 100 cycles, which is better than the case of Sn–Cu films in our previous study. This is originated from the formation of an appropriate buffer matrix for the large volume change, by the electrochemical decomposition of the needle-like $NiSn_3$ phase into Ni_3Sn_4 fine particles and the dispersion of these particles in the β-Sn layer. In contrast, for the 2h- and 10h-annealed films, a thicker Ni_3Sn_4 layer was formed due to the progress of alloying, and this layer collapsed and became electrically isolated during cycling, leading to the poor cycleability of the films. Although this result was different from our expectation, it was suggested that the Ni_3Sn_4 phase acts as a buffer only in the case of fine particles, both in the electrodeposited tin film and the composite electrodes. Therefore, the composite electrodes utilizing β-Sn and Ni_3Sn_4 fine particles will show good charge–discharge characteristics. In addition, the 25h-annealed film showed very low capacity, less than 5 mAh $(g\text{-}Sn)^{-1}$, which indicates that Ni_3Sn_4 is almost inactive with sodium. Therefore, Ni_3Sn_4 phase is suitable as a buffer for the large volume change of β-Sn.

As a conclusion, the 0h-annealed Sn–Ni film showed reasonably high reversible

capacities and good cycleability, and thus the Sn–Ni system is a good candidate as a negative electrode material for sodium secondary battery.

Acknowledgments

This study was partly supported by the Advanced Low Carbon Technology Research and Development Program (ALCA) of Japan Science and Technology Agency (JST), and MEXT program "Elements Strategy Initiative to Form Core Research Center" (since 2012), MEXT; Ministry of Education Culture, Sports, Science and Technology, Japan.

References

[1] S.W. Kim, D.H. Seo, X. Ma, G. Ceder, and K. Kang, Electrode Materials for Rechargeable Sodium-Ion Batteries: Potential Alternatives to Current Lithium-Ion Batteries, Adv. Energy Mater. 2 (2012) 710–721.

[2] V. Palomares, M. Casas-Cabanas, E. Castillo-Martínez, M.H. Han, T. Rojo, Update on Na-based battery materials. A growing research path, Energy Environ. Sci. 6 (2013) 2312–2337.

[3] N. Yabuuchi, K. Kubota, M. Dahbi, and S. Komaba, Research Development on Sodium-Ion Batteries, Chem. Rev. 114 (2014) 11636–11682.

[4] D. Kundu, E. Talaie, V. Duffort, and L.F. Nazar, The Emerging Chemistry of Sodium Ion Batteries for Electrochemical Energy Storage, Angew. Chem. Int. Ed. 54 (2015) 3431–3448.

[5] S. Komaba, W. Murata, T. Ishikawa, N. Yabuuchi, T. Ozeki , T. Nakayama, A. Ogata, K. Gotoh, K. Fujiwara, Electrochemical Na Insertion and Solid Electrolyte Interphase for Hard-Carbon Electrodes and Application to Na-Ion Batteries, Adv. Funct. Mater. 21(2011) 3859–3867.

[6] P. Senguttuvan, G. Rousse, V. Seznec, J.M. Tarascon, M.R. Palacín, $Na_2Ti_3O_7$: Lowest Voltage Ever Reported Oxide Insertion Electrode for Sodium Ion Batteries, Chem. Mater. 23 (2011) 4109–4111.

[7] S. Il Park, I. Gocheva, S. Okada, J. Yamaki, Electrochemical Properties of $NaTi_2(PO_4)_3$ Anode for Rechargeable Aqueous Sodium-Ion Batteries, J. Electrochem. Soc. 158 (2011) A1067–A1070.

[8] R. Hagiwara, K. Tamaki, K. Kubota, T. Goto, T. Nohira, Thermal Properties of Mixed Alkali Bis(trifluoromethylsulfonyl)amides, J. Chem. Eng. Data 53 (2008) 355–358.

[9] K. Kubota, K. Tamaki, T. Nohira, T. Goto, R. Hagiwara, Electrochemical properties of alkali bis(trifluoromethylsulfonyl)amides and their eutectic mixtures, Electrochim. Acta 55 (2010) 1113–1119.

[10] K. Kubota, T. Nohira, T. Goto, R. Hagiwara, Novel inorganic ionic liquids possessing low melting temperatures and wide electrochemical windows: Binary mixtures of alkali bis(fluorosulfonyl)amides, Electrochem. Commun. 10 (2008) 1886–1888.

[11] K. Kubota, T. Nohira, R. Hagiwara, Thermal Properties of Alkali Bis(fluorosulfonyl)amides and Their Binary Mixtures, J. Chem. Eng. Data 55 (2010) 3142–3146.

[12] T. Nohira, T. Ishibashi, R. Hagiwara, Properties of an intermediate temperature ionic liquid NaTFSA–CsTFSA and charge–discharge properties of $NaCrO_2$ positive electrode at 423 K for a sodium secondary battery, J. Power Sources 205 (2012) 506–509.

[13] A. Fukunaga, T. Nohira, Y. Kozawa, R. Hagiwara, S. Sakai, K. Nitta, S. Inazawa, Intermediate–temperature ionic liquid NaFSA–KFSA and its application to sodium secondary batteries, J. Power Sources 209 (2012) 52–56.

[14] C.Y. Chen, K. Matsumoto, T. Nohira, R. Hagiwara, A. Fukunaga, S. Sakai, K. Nitta, Shinji Inazawa, Electrochemical and structural investigation of $NaCrO_2$ as a positive electrode for sodium secondary battery using inorganic ionic liquid NaFSA–KFSA, J. Power Sources 237 (2013) 52–57.

[15] C.Y. Chen, K. Matsumoto, T. Nohira, R. Hagiwara, Y. Orikasa, Y. Uchimoto, Pyrophosphate $Na_2FeP_2O_7$ as a low-cost and high-performance positive electrode material for sodium secondary batteries utilizing an inorganic ionic liquid, J. Power Sources 246 (2013) 783–787.

[16] T.B. Massalski, Binary Alloy Phase Diagrams second ed., ASM International, Ohio, 1990.

[17] V.L. Chevrier, G. Ceder, Challenges for Na-ion Negative Electrodes, J. Electrochem. Soc. 158 (2011) A1011–A1014.

[18] T. Yamamoto, T. Nohira, R. Hagiwara, A. Fukunaga, S. Sakai, K. Nitta, S. Inazawa, Charge–discharge behavior of tin negative electrode for a sodium secondary battery using intermediate temperature ionic liquid sodium bis(fluorosulfonyl)amide–potassium bis(fluorosulfonyl)amide, J. Power Sources 217 (2012) 479–484.

[19] T. Yamamoto, T. Nohira, R. Hagiwara, A. Fukunaga, S. Sakai, K. Nitta, S. Inazawa, Thermodynamic studies on Sn–Na alloy in an intermediate temperature ionic liquid NaFSA–KFSA at 363 K, J. Power Sources 237 (2013) 98–103.

[20] T. Yamamoto, T. Nohira, R. Hagiwara, A. Fukunaga, S. Sakai, K. Nitta, S. Inazawa, Improved cyclability of Sn–Cu film electrode for sodium secondary battery using inorganic ionic liquid electrolyte, Electrochim. Acta 135 (2014) 60–67.

[21] W.J. Zhang, A review of the electrochemical performance of alloy anodes for lithium-ion batteries, J. Power Sources 196 (2011) 13–24.

[22] S. Komaba, Y. Matsuura, T. Ishikawa, N. Yabuuchi, W. Murata, S. Kuze, Redox reaction of Sn-polyacrylate electrodes in aprotic Na cell, Electrochem. Commun. 21 (2012) 65–68.

[23] L.D. Ellis, T.D. Hatchard, M.N. Obrovac, Reversible Insertion of Sodium in Tin, J. Electrochem. Soc. 159 (2012) A1801–A1805.

[24] L. Baggetto, P. Ganesh, R.P. Meisner, R.R. Unocic, J.C. Jumas, C.A. Bridges, G.M. Veith, Characterization of sodium ion electrochemical reaction with tin anodes: Experiment and theory, J. Power Sources 234 (2013) 48–59.

[25] Z. Du, R.A. Dunlap, M.N. Obrovac, Investigation of the reversible sodiation of Sn foil by ex-situ X-ray diffractometry and Mössbauer effect spectroscopy, J. Alloys Compd. 617 (2014) 271–276.

[26] L. Xiao, Y. Cao, J. Xiao, W. Wang, L. Kovarik, Z. Nie, J. Liu, High capacity, reversible alloying reactions in SnSb/C nanocomposites for Na-ion battery applications, Chem. Commun. 48 (2012) 3321–3323.

[27] L. Baggetto, J.C. Jumas, J. Górka, C.A. Bridges, G.M. Veith, Predictions of particle size and lattice diffusion pathway requirements for sodium-ion anodes using η-Cu_6Sn_5 thin films as a model system, Phys. Chem. Chem. Phys. 15 (2013) 10885–10894.

[28] Y.M. Lin, P.R. Abel, A. Gupta, J.B. Goodenough, A. Heller, C.B. Mullins, Sn–Cu Nanocomposite Anodes for Rechargeable Sodium-Ion Batteries, Appl. Mater. Interfaces 5 (2013) 8273–8277.

[29] L.D. Ellis, P.P. Ferguson, M.N. Obrovac, Sodium Insertion into Tin Cobalt Carbon Active/Inactive Nanocomposite, J. Electrochem. Soc 160 (2013) A869–A872.

[30] P.R. Abel, M.G. Fields, A. Heller, and C.B. Mullins, Tin−Germanium Alloys as Anode Materials for Sodium-Ion Batteries, ACS Appl. Mater. Interfaces 6 (2014) 15860–15867.

[31] J. Liu, Y. Wen, P.A. van Aken, J. Maier, and Y. Yu, Facile Synthesis of Highly Porous Ni–Sn Intermetallic Microcages with Excellent Electrochemical Performance for Lithium and Sodium Storage, Nano Lett. 14 (2014) 6387−6392.

[32] Y. Kim, Y. Kim, Y. Park, Y.N. Jo, Y.J. Kim, N.S. Choi, and K.T. Lee, SnSe alloy as a promising anode material for Na-ion batteries, Chem. Commun. 51 (2015) 50–53.

[33] Y. Wang, D. Su, C. Wang, G. Wang, SnO_2@MWCNT nanocomposite as a high capacity anode material for sodium-ion batteries, Electrochem. Commun. 29 (2013) 8–11.

[34] M. Shimizu, H. Ushui, H. Sakaguchi, Electrochemical Na-insertion/extraction properties of SnO thick-film electrodes prepared by gas-deposition, J. Power Sources 248 (2014) 378–382.

[35] L. Wu, X. Hu, J. Qian, F. Pei, F. Wu, R. Mao, X. Ai, H. Yang, Y. Cao, A Sn–SnS–C nanocomposite as anode host materials for Na-ion batteries, J. Mater. Chem. A 1 (2013) 7181–7184.

[36] B. Qu, C. Ma, G. Ji, C. Xu, J. Xu, Y.S. Meng, T. Wang, and J.Y. Lee, Layered SnS_2-Reduced Graphene Oxide Composite – A High-Capacity, High-Rate, and Long-Cycle Life Sodium-Ion Battery Anode Material, Adv. Mater. 26 (2014) 3854–3859.

[37] W. Li, S.L. Chou, J.Z. Wang, J.H. Kim, H.K. Liu, and S.X. Dou, $Sn_{4+x}P_3$ @ Amorphous Sn-P Composites as Anodes for Sodium-Ion Batteries with Low Cost, High Capacity, Long Life, and Superior Rate Capability, Adv. Mater. 26 (2014) 4037–4042.

[38] J. Qian, Y. Xiong, Y. Cao, X. Ai, and H. Yang, Synergistic Na-Storage Reactions in Sn_4P_3 as a High-Capacity, Cycle-stable Anode of Na-Ion Batteries, Nano Lett. 14 (2014) 1865−1869.

[39] H. Mukaibo, T. Sumi, T. Yokoshima, T. Momma, and T. Osaka, Electrodeposited Sn-Ni Alloy Film as a High Capacity Anode Material for Lithium-Ion Secondary Batteries, Electrochem. Solid-State Lett. 6 (2003) A218–A220.

[40] J. Hassoun, S. Panero, B. Scrosati, Electrodeposited Ni–Sn intermetallic electrodes for advanced lithium ion batteries, Journal of Power Sources 160 (2006) 1336–1341.

[41] N. Tamura, R. Ohshita, M. Fujimoto, S. Fujitani, M. Kamino, I. Yonezu, Study on the anode behavior of Sn and Sn–Cu alloy thin-film electrodes, J. Power Sources 107 (2002) 48–55.

[42] N. Tamura, R. Ohshita, M. Fujimoto, M. Kamino, and S. Fujitani, Advanced Structures in Electrodeposited Tin Base Negative Electrodes for Lithium Secondary Batteries, J. Electrochem. Soc. 150 (2003) A679–A683.

[43] W. Zhang, Growth Behavior of Meta-Stable $NiSn_3$ Intermetallic Compound and Its Potential Influence on the Reliability of Electronic Components, IEEE Transactions on Components, Packaging, and Manufacturing Technology 1 (2011) 1259–1268.

[44] O. Mao and J.R. Dahn, Mechanically Alloyed Sn-Fe(-C) Powders as Anode Materials for Li-Ion Batteries, J. Electrochem. Soc. 146 (1999) 414–422.

[45] D.R. Frear, F.M. Hosking, and P.T. Vianco, Mechanical Behavior of Solder Joint Interfacial Intermetallics, Materials developments in microelectronic packaging, P.J. Singh, ed., ASM International, Metals park, Ohio (1991) 229–240.

[46] P.F. Yang, Y.S. Lai, S.R. Jian, J. Chen, R.S. Chen, Nanoindentation identifications of mechanical properties of Cu_6Sn_5, Cu_3Sn, and Ni_3Sn_4 intermetallic compounds derived by diffusion couples, Mater. Sci. Eng. A 485 (2008) 305–310.

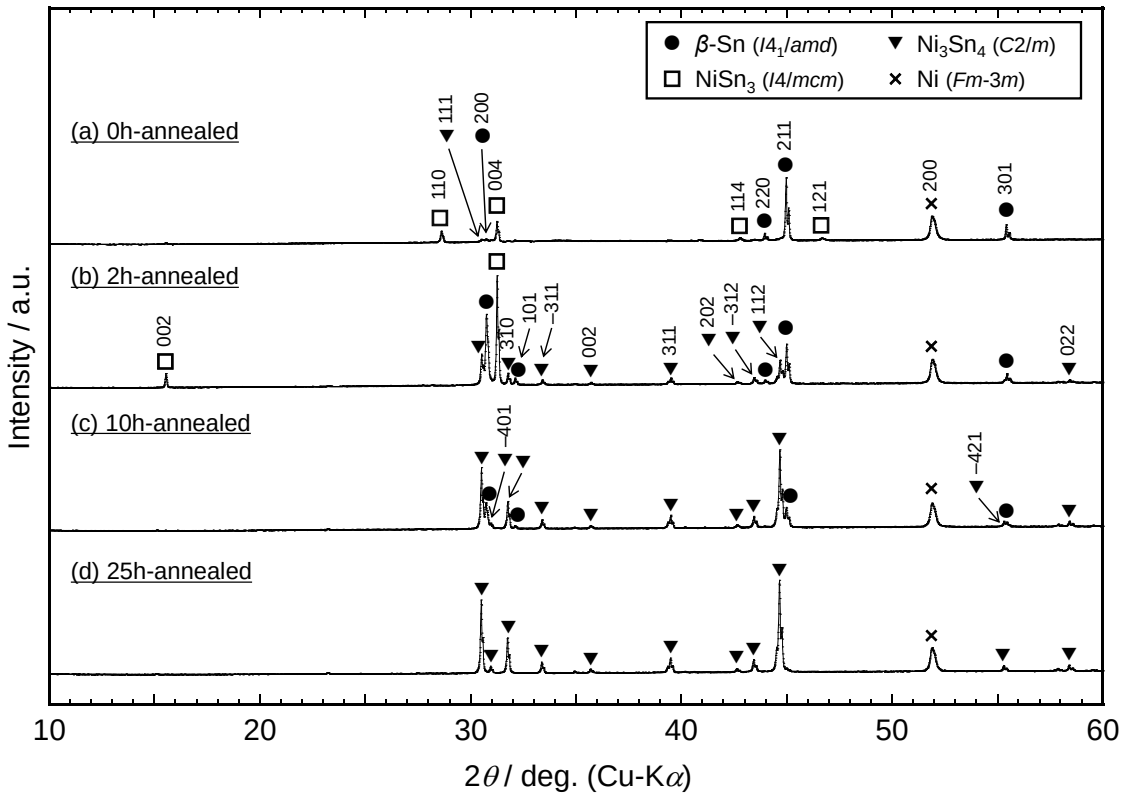

Fig. 1. XRD patterns of annealed Sn–Ni alloy films. Annealing temperature: 463 K. Annealing time: 0–25 h.

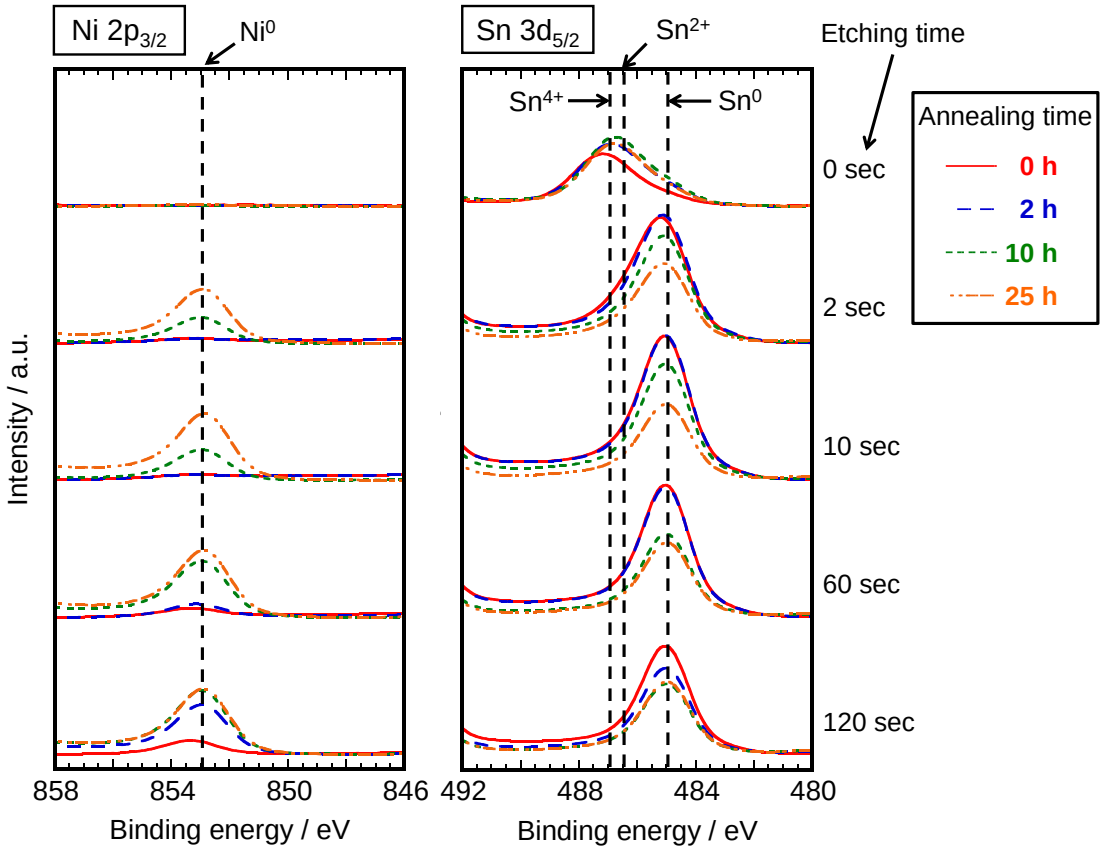

Fig. 2. XPS depth profiles of annealed Sn–Ni alloy films. Annealing time: 0–25 h.

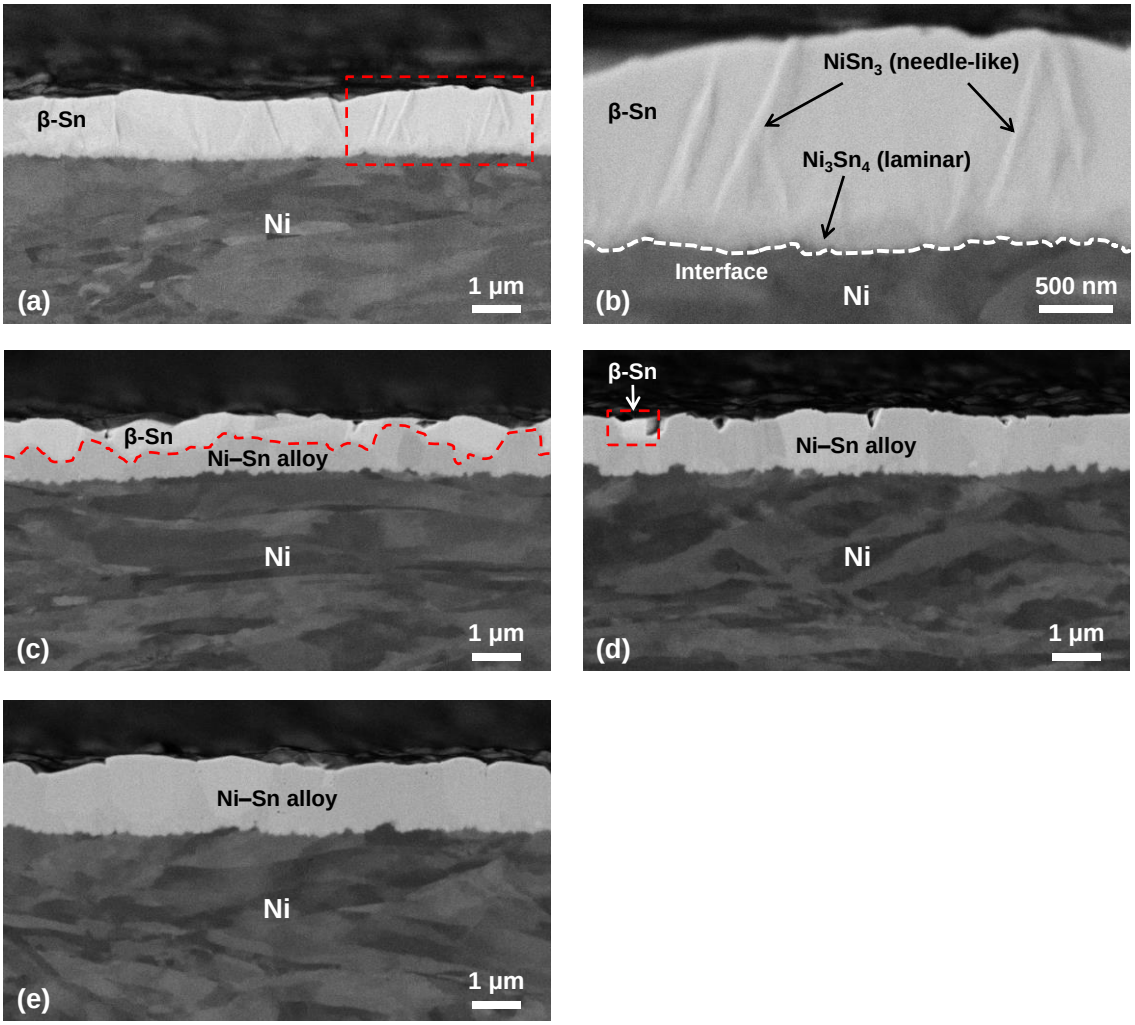

Fig. 3. Selected cross-sectional FE-SEM images of annealed Sn–Ni alloy films. (a) and (b) 0h-annealed film at different magnifications, (c) 2h-annealed film, (d) 10h-annealed film, and (e) 25h-annealed film. (b) shows an enlarged view of the red rectangular area shown in (a).

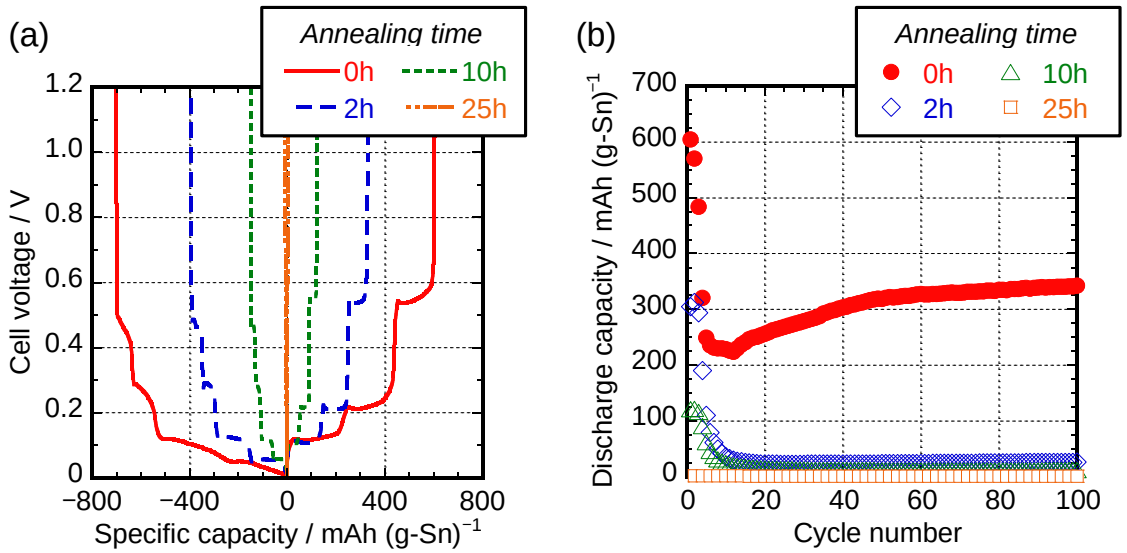

Fig. 4. (a) Initial charge–discharge curves of annealed Sn–Ni alloy films at a current density of 84.7 mA (g-Sn)$^{-1}$. (b) Cycle characteristics of these Sn–Ni films for 100 cycles.

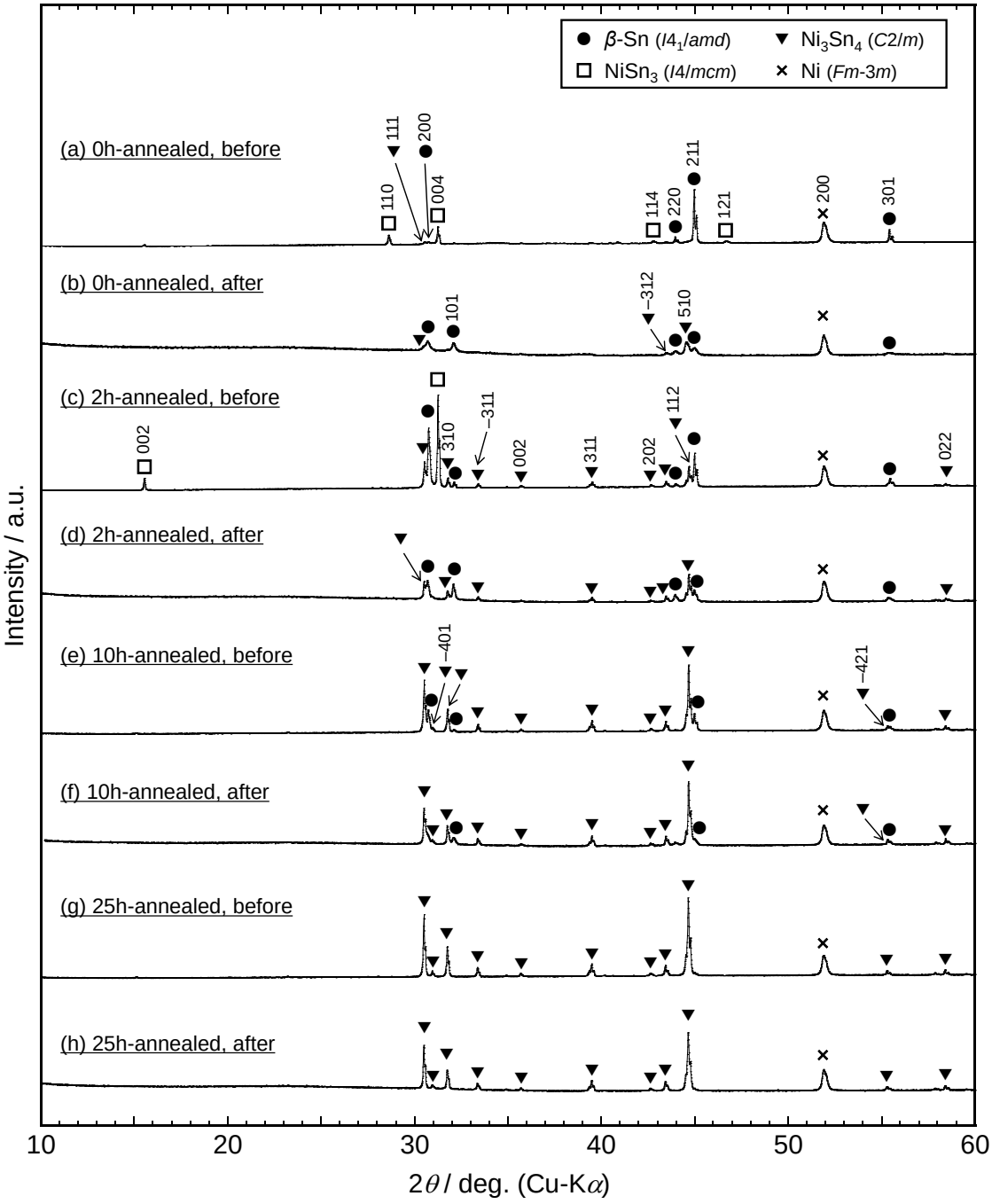

Fig. 5. Comparison of the XRD patterns of Sn–Ni film electrodes before and after charge–discharge tests. (a) 0h-annealed, before, (b) 0h-annealed, after, (c) 2h-annealed, before, (d) 2h-annealed, after, (e) 10h-annealed film, before, (f) 10h-annealed film, after, (g) 25h-annealed film, before, and (h) 25h-annealed film, after.

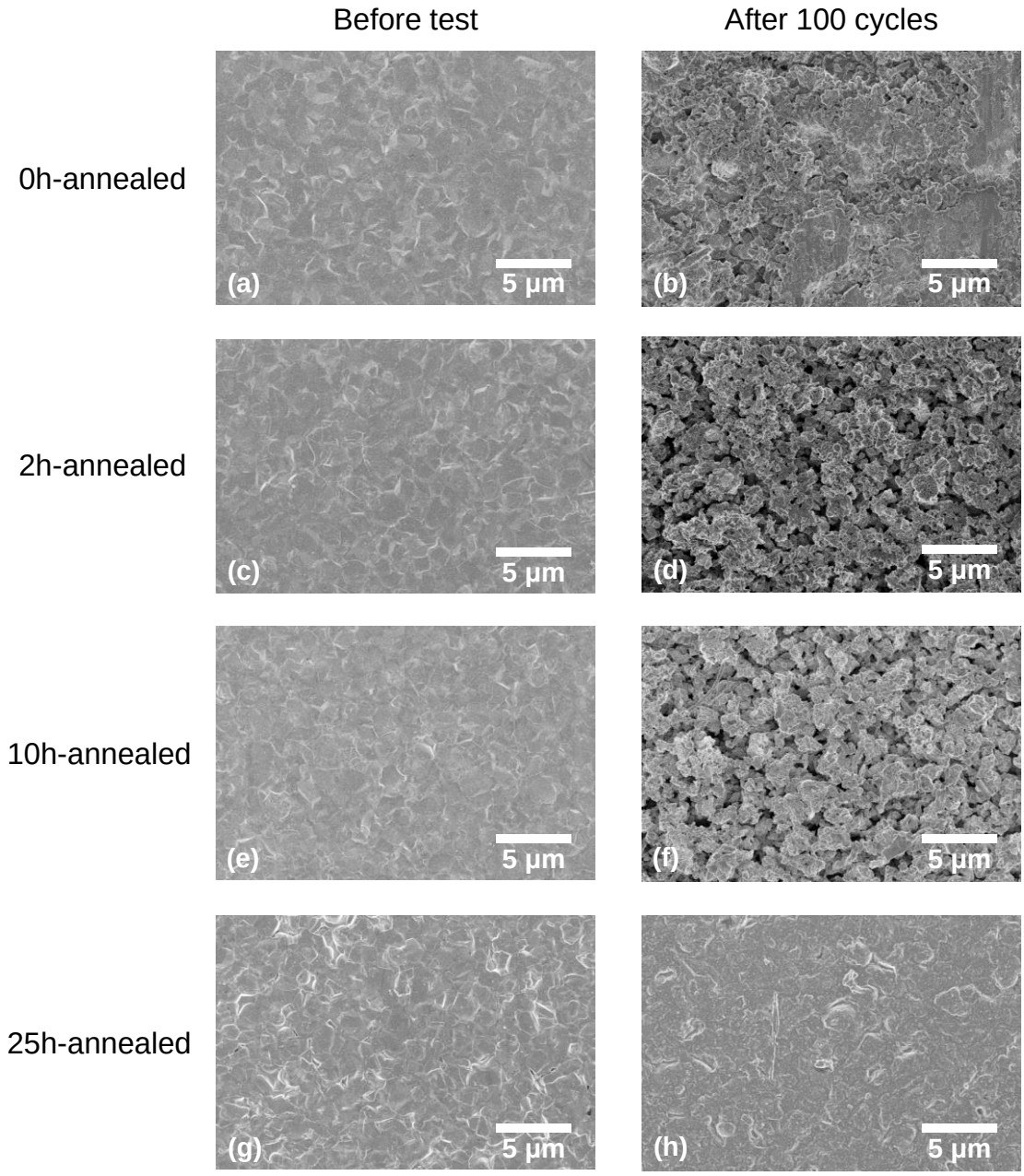

Fig. 6. Representative surface SEM images of Sn–Ni film electrodes before and after charge–discharge tests. (a) 0h-annealed, before, (b) 0h-annealed, after, (c) 2h-annealed, before, (d) 2h-annealed, after, (e) 10h-annealed film, before, (f) 10h-annealed film, after, (g) 25h-annealed film, before, and (h) 25h-annealed film, after.

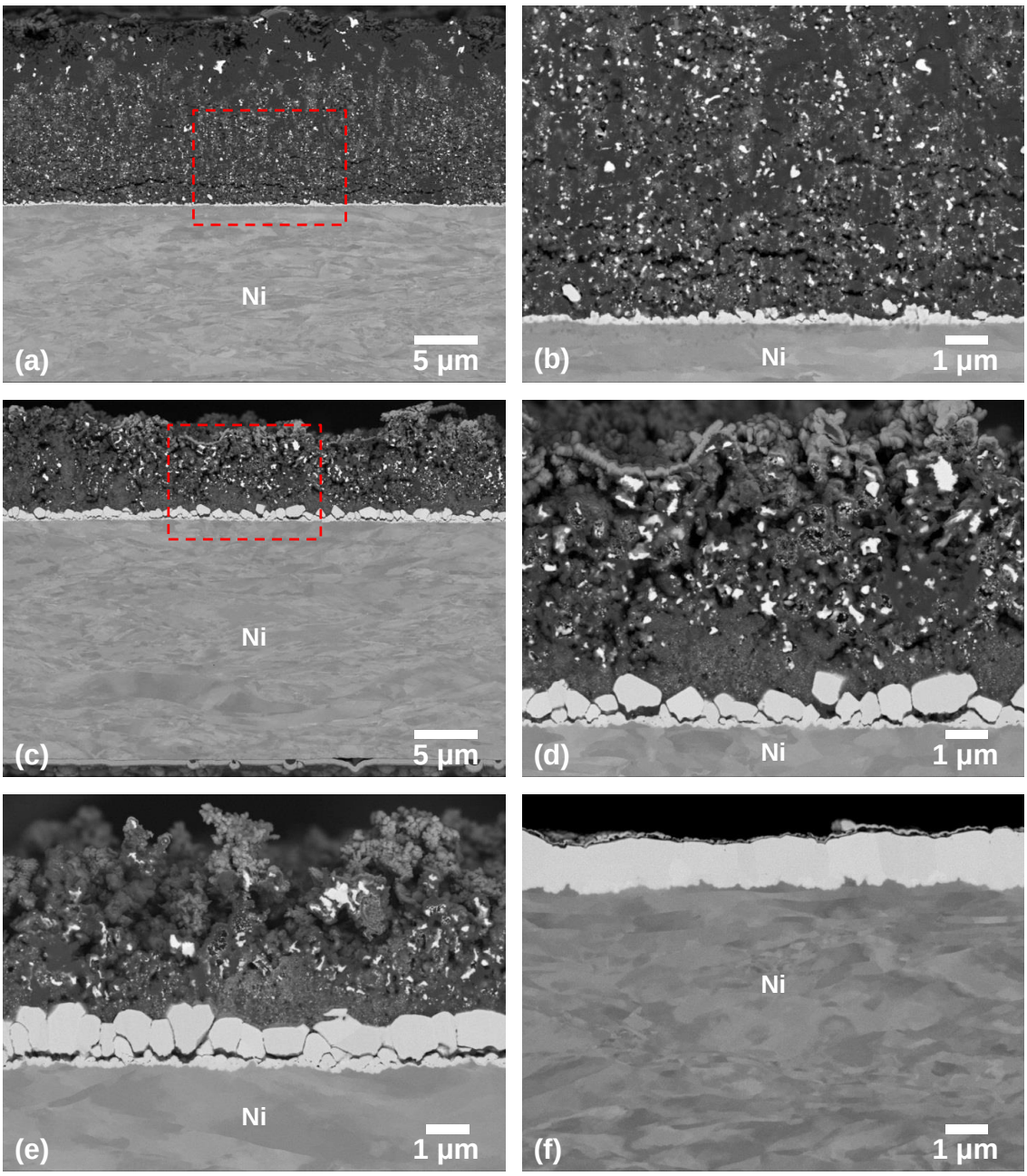

Fig. 7. Representative cross-sectional SEM images of Sn–Ni film electrodes after charge–discharge tests. (a) and (b) 0h-annealed film at different magnifications, (c) and (d) 2h-annealed film at different magnifications, (e) 10h-annealed film, and (f) 25h-annealed film. (b) and (d) show enlarged views of the red rectangular areas shown in (a) and (c), respectively.